Radio Science

METHOD

10.1029/2024RS007957

Multi-Frequency SuperDARN Interferometer Calibration

E. G. Thomas[1], S. G. Shepherd[1], and G. Chisham[2]

[1]Dartmouth College, Hanover, NH, USA, [2]British Antarctic Survey, Cambridge, UK

Key Points:

- Calibration of Super Dual Auroral Radar Network (SuperDARN) interferometer angle of arrival data remains an outstanding challenge
- Analysis of data at multiple frequencies can overcome the inherent 2π measurement ambiguity in the time delay correction factor (t_{diff})
- Example applications are shown for historical and contemporary multi-frequency SuperDARN observations

Supporting Information:

Supporting Information may be found in the online version of this article.

Correspondence to:

E. G. Thomas,
evan.g.thomas@dartmouth.edu

Citation:

Thomas, E. G., Shepherd, S. G., & Chisham, G. (2024). Multi-frequency SuperDARN interferometer calibration. *Radio Science*, *59*, e2024RS007957. https://doi.org/10.1029/2024RS007957

Received 26 JAN 2024
Accepted 3 JUL 2024

Abstract The ground-based, high-frequency radars of the Super Dual Auroral Radar Network (SuperDARN) observe backscatter from ionospheric field-aligned plasma irregularities and features on the Earth's surface out to ranges of several thousand kilometers via over-the-horizon propagation of transmitted radio waves. Interferometric techniques can be applied to the received signals at the primary and secondary antenna arrays to measure the vertical angle of arrival, or elevation angle, for more accurate geolocation of SuperDARN observations. However, the calibration of SuperDARN interferometer measurements remains challenging for several reasons, including a 2π phase ambiguity when solving for the time delay correction factor needed to account for differences in the electrical path lengths between signals received at the two antenna arrays. We present a new technique using multi-frequency ionospheric and ground backscatter observations for the calibration of SuperDARN interferometer data, and demonstrate its application to both historical and recent data.

1. Introduction

The Super Dual Auroral Radar Network (SuperDARN) is an international collaboration of ground-based, high-frequency (HF) radars monitoring space weather conditions in the Earth's ionosphere and lower thermosphere (Chisham et al., 2007; Greenwald et al., 1995; Nishitani et al., 2019). Most SuperDARN radars have a smaller interferometer antenna array (4 elements), displaced from the main antenna array (16 elements) by ∼60–185 m, to measure the vertical angle of arrival, or elevation angle, of the received radar signals (Baker & Greenwald, 1988; McDonald et al., 2013; Milan et al., 1997; Shepherd, 2017). These elevation angle measurements are important for the accurate geolocation of SuperDARN backscatter observations, both from field-aligned ionospheric irregularities used to map two-dimensional plasma flow (e.g., Bristow et al., 2022; Cousins et al., 2013; Fiori et al., 2010; Ruohoniemi & Baker, 1998) and from ground irregularities on the Earth's land and sea surfaces (e.g., Greenwald et al., 2017; Greenwood et al., 2011; Ponomarenko et al., 2010; Shand et al., 1998).

In SuperDARN radar systems, the physical separation between the main and interferometer antenna arrays introduces a phase delay in the signals that are received by each antenna that depends on the elevation angle. In addition, there are typically differences in the electrical path lengths from the two antenna arrays to the point at which the return signals are correlated. The corresponding difference in the signal travel time along each path, known as t_{diff}, causes a systematic offset in the measured phase difference between the signals from the two arrays, which must be accounted for (Chisham et al., 2021, and references therein).

While it is possible to measure these electrical path differences, it can be challenging to routinely do so at remote sites and cannot be performed for historical data sets. Several methods have therefore been developed to estimate t_{diff} using ionospheric scatter (IS) or ground scatter (GS) measurements assumed to follow known propagation characteristics, for example, from meteor trails (Chisham, 2018; Chisham & Freeman, 2013), $\frac{1}{2}$-hop *E*-region IS (Ponomarenko et al., 2018), 1-hop *F*-region GS (Ponomarenko et al., 2015), or targets with a known ground location such as artificially generated irregularities (Burrell et al., 2016). However, because SuperDARN radars typically operate at only one or two frequencies, these techniques are susceptible to a 2π ambiguity when estimating t_{diff} and therefore may not identify the true value that is valid across all possible operating frequencies (assuming one exists).

To address this issue, we have extended the "virtual height method" described by Chisham et al. (2021) to utilize multi-frequency observations of both IS and GS echoes for the calibration of t_{diff}. The methodology of this multi-frequency approach is described in Section 2. In Sections 3 and 4 we demonstrate the application of this technique to historical SuperDARN data, as well as provide contemporary t_{diff} estimates for selected radars. In Section 5 we compare the t_{diff} estimates from our approach with the meteor calibration method of Chisham (2018). In Section 6 we discuss our results from applying the multi-frequency technique.

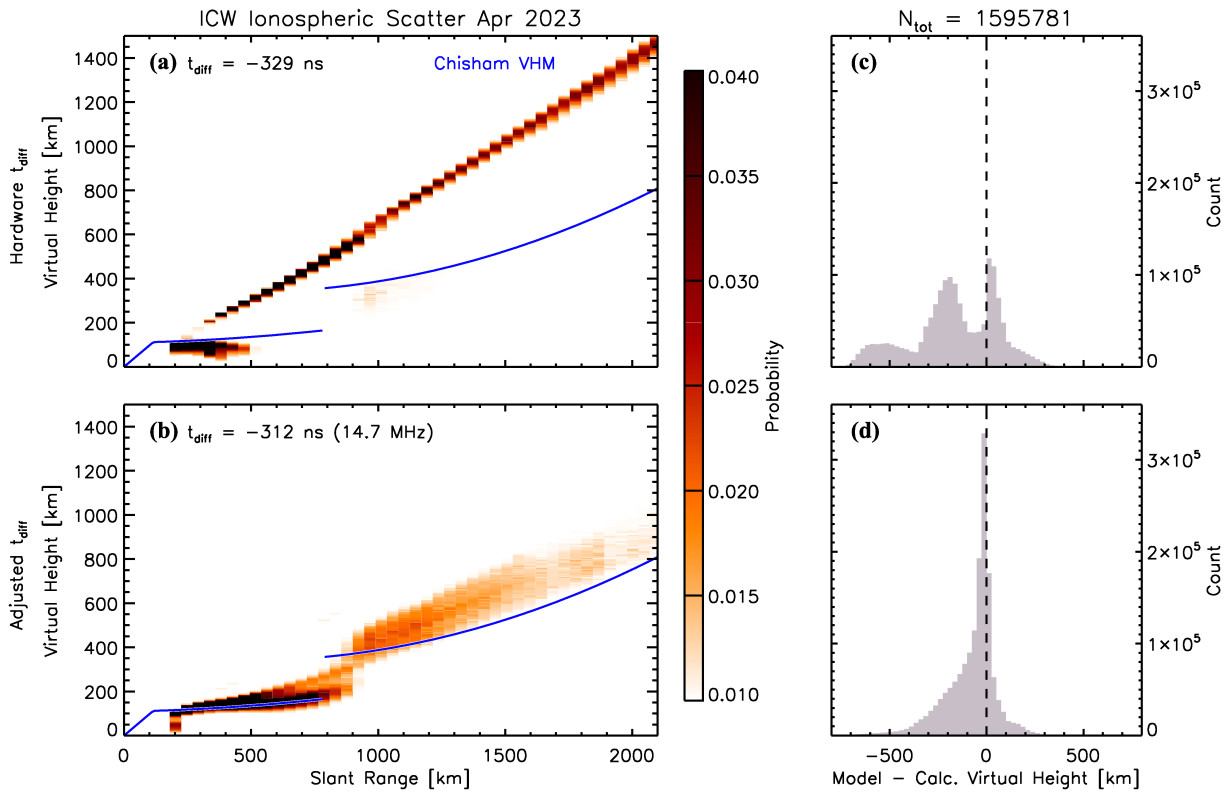

Figure 1. (a) Virtual height distribution observed by the Iceland West (ICW) SuperDARN radar at 14.7 MHz from the entire month of April 2023 for ranges 0–2,100 km when using the initial t_{diff} estimate (−329 ns), with the Chisham VHM overlaid in blue. (b) Virtual height distribution found by adjusting the $\frac{1}{2}$-hop ionospheric backscatter to match the Chisham VHM (−312 ns). Panels (c and d) show histograms of the difference between the modeled and measured virtual heights at these same ranges. After Figure 1 of Chisham et al. (2021).

2. Methodology

The virtual height comparison method introduced by Chisham et al. (2021) is based on the presumption that, for a correct t_{diff} value, the observed elevation angle (or virtual height) variations with range should qualitatively match the behavior of an empirical virtual height model (VHM). These VHMs are the default method for geolocation of line-of-sight (LOS) SuperDARN observations and are required for use at radar sites that either do not have an interferometer antenna array or t_{diff} has not yet been calibrated (e.g., Chisham et al., 2008; Thomas & Shepherd, 2022). Chisham et al. (2021) demonstrated how, for $\frac{1}{2}$-hop IS, an obviously incorrect t_{diff} value can be adjusted until the observed distribution of slant range and virtual height align with the VHM of Chisham et al. (2008) (hereafter referred to as the Chisham VHM).

As an example, we apply this virtual height calibration technique to the recently constructed Iceland West (ICW) SuperDARN radar that, along with the co-located Iceland East radar, saw first light in January 2023. An initial t_{diff} estimate of −329 ns was determined for ICW based on the difference in coaxial cable lengths from the main and interferometer antenna arrays to a central equipment shelter housing the radar electronics. Figure 1a shows the joint probability distribution of IS observed by ICW during the entire month of April 2023 at a single frequency (14.7 MHz) divided into 45 km range and 5 km height bins, with the Chisham VHM overlaid in blue. Note the distributions are normalized by the maximum occurrence at each range bin, after Chisham et al. (2008, 2021). Here we separate IS and GS echoes using the default SuperDARN criterion:

$$|v| + \frac{w}{3} < 30 \text{ m s}^{-1} \quad (1)$$

where v is the fitted Doppler velocity and w is the spectral width. We will address the impact of potentially misclassified scatter in Section 6.

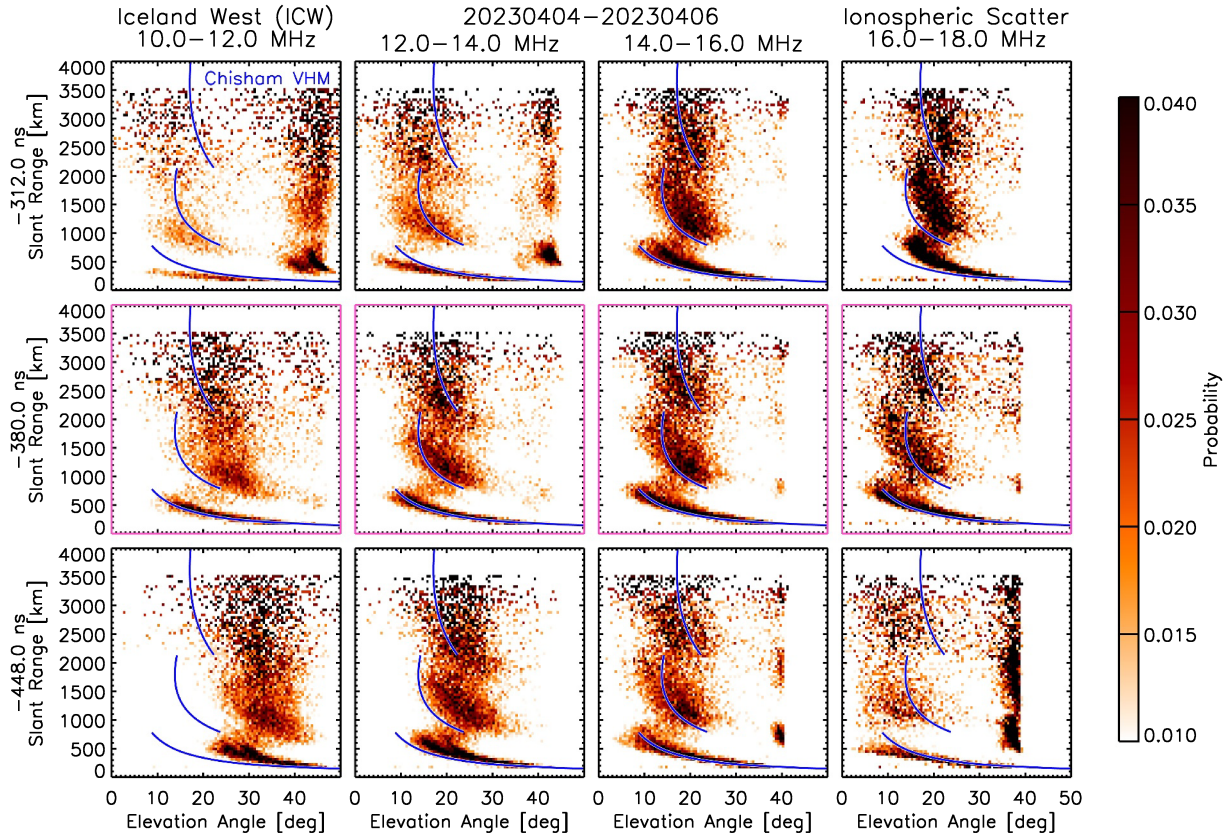

Figure 2. Joint probability distributions of elevation angle and slant range for ionospheric scatter observed by ICW on 4–6 April 2023 in 0.5° elevation and 45 km range bins, sorted by radar operating frequency into four bands between 10 MHz (left column) and 18 MHz (right column) and calculated using three values of t_{diff}: −312 ns (top row), −380 ns (middle), and −448 ns (bottom). The Chisham et al. (2008) empirical virtual height model is overlaid on each panel in blue.

Beyond ∼500 km range, all of the data in Figure 1a are mapped to very large and linearly increasing virtual heights, suggesting the initial t_{diff} estimate is incorrect. The histogram in Figure 1c shows that the distribution of differences between the VHM and calculated virtual heights has multiple peaks: the peak near zero is likely due to the near-range *E*-region echoes where the virtual heights are small, while the other two peaks at larger negative values are likely attributable to the $\frac{1}{2}$-hop *F*-region echoes at farther ranges where the calculated virtual heights are much greater than the model suggests. Figure 1b shows the same data using a revised t_{diff} value of −312 ns where the calculated virtual heights now align much more closely with the Chisham VHM predictions in both the $\frac{1}{2}$-hop *E*- and *F*-region regimes. The corresponding histogram in Figure 1d confirms this improved agreement with a single-peaked distribution maximizing near zero and a tail toward negative values. This tail can again be attributed to $\frac{1}{2}$-hop *F*-region echoes with greater virtual heights than the Chisham VHM predicts.

In Figure 2 we consider multi-frequency data observed by ICW with a special sounding mode over 3 days in April 2023, with each of the four columns corresponding to a 2 MHz frequency band between 10 and 18 MHz. Note the ICW radar was actually operating at 8 equally-spaced frequencies from 9.6 to 16.6 MHz at 1 MHz increments; more details about this special sounding mode are provided in Section 4. Each panel in Figure 2 shows joint probability distributions of the observed IS divided into 0.5° elevation and 45 km range bins. A different t_{diff} value is used in each row to calculate the elevation angles: −312, −380, and −448 ns. The differences between the t_{diff} values applied to each row are a multiple of 68 ns, or one wavelength at 14.7 MHz (i.e., near the center of the 2 MHz frequency band in the third column), to illustrate the 2π ambiguity when estimating t_{diff}. Note that −312 ns (top row) was the value previously identified with the virtual height comparison method at 14.7 MHz in Figure 1, and overlaid on all of the panels in blue is the Chisham VHM.

In the third column of Figure 2 (14–16 MHz) the elevation-range distributions appear nearly identical regardless of which of the three t_{diff} values are used. Specifically, the near-range echoes in all three panels closely follow the

VHM curve corresponding to $\frac{1}{2}$-hop backscatter from *E*-region irregularities. However for the other frequency bands, the elevation-range distributions in each of the three rows no longer agree with one another. Only when calculating elevation angles using the t_{diff} value from the center row (−380 ns, pink outline) do the distributions behave similarly at each frequency band while also qualitatively aligning with the Chisham VHM at all observed ranges. This improvement in the model/data alignment suggests that all frequencies are well represented by the new t_{diff} value.

While this tuning procedure may be performed manually to find the optimal t_{diff} value for all frequency bands, in practice an automated procedure is desirable given the large data set from the more than 30 continuously operating SuperDARN radars. Here we describe a simple two-step minimization procedure that has been found to quickly determine the appropriate t_{diff}, examples of which are shown in the following sections.

First, we organize the observations from a given radar according to operating frequency. Typically we select bin sizes of 2 MHz spanning from 8 to 18 MHz, depending on the available frequency distribution; using a frequency resolution smaller than 1 MHz comes at significant computational cost and has not shown an improvement in calibration performance. Ideally, the upper and lower frequency bounds should be separated by at least 5 MHz to ensure this technique's ability to fully resolve the 2π ambiguity when estimating t_{diff} (see Section 4 for more details).

In the first stage of the minimization process, we calculate elevation angles using the generalized algorithm of Shepherd (2017) for each frequency bin and each value of t_{diff} over the range −1,000 to +1,000 ns at steps of 5 ns. This search range of ±1,000 ns is based on the maximum physical distance between the main and interferometer antenna arrays, as well as the largest t_{diff} value currently listed in the SuperDARN analysis software (−498 ns). Using the median difference between the values of a VHM and the calculated elevation angles for each frequency bin, we select the t_{diff} value with the minimum total of median differences for all frequency bins. The second step is to repeat the minimization process over a smaller range (±10 ns) centered about the t_{diff} value determined in the first step, using 1 ns steps. As with the frequency bin selection, a finer resolution in t_{diff} may be applied at each stage at the expense of increased computational time.

Note there are currently three available SuperDARN VHMs: the "standard" VHM (Greenwald et al., 1985), the Chisham VHM, and the Christmas Valley VHM (Thomas & Shepherd, 2022, hereafter referred to as the CV VHM). Both the standard and Chisham VHMs are restricted to IS only, while the CV VHM has separate models for IS and GS propagation modes. In the next sections we use the CV VHM rather than the Chisham VHM to allow inclusion of both IS and GS observations in our analysis.

3. Common Mode Data

To our knowledge, the earliest available multi-frequency SuperDARN observations with quality interferometer data were collected by the Goose Bay radar (GBR) during standard operations from January to March 1994 on four frequency bands: 11.5–12.0, 12.3–13.0, 14.4–14.9, and 16.4–16.9 MHz. Figure 3 shows joint probability distributions of (top) IS and (bottom) GS observations by GBR during this 3-month interval divided into 0.5° elevation and 45 km range bins and normalized in the same fashion as Figure 2. Each column corresponds to a different frequency band, and the CV VHM is overlaid on each panel in blue for reference.

The elevation angles in Figure 3 are calculated using the t_{diff} value of 487 ns listed for GBR in the SuperDARN analysis software for these dates (SuperDARN Data Analysis Working Group et al., 2022). While observations from a high-latitude radar such as GBR are not expected to perfectly align with the CV VHM (which was derived from mid-latitude observations), the data and model curves do not agree for any of the four frequency bands. More importantly, all but the nearest range data are mapped to very high elevation angles, which Chisham et al. (2021) demonstrated to be a likely symptom of an incorrect t_{diff} value (e.g., Figure 1a).

Applying the multi-frequency calibration technique suggests a t_{diff} value of 457 ns, the result of which can be seen in Figure 4. Here we see the IS and GS measurements are now much better aligned with the CV VHM at all four frequency bands, with a few notable exceptions. The GS distributions in both the 10–12 MHz (Figure 4e) and 16–18 MHz (Figure 4h) bands show the opposite behavior for ranges beyond 1,500 km and elevation angles above 20°, with elevation increasing instead of decreasing at farther ranges. These regions are likely associated with observations from the backlobe, which is a well-known characteristic of the log-periodic antenna design used by

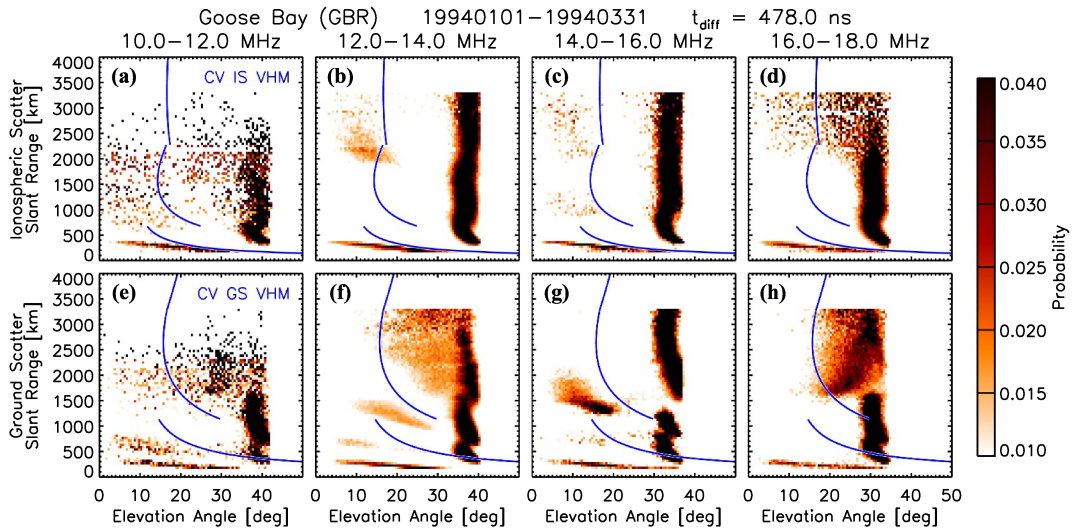

Figure 3. Joint probability distributions of elevation angle and slant range for (top) ionospheric scatter and (bottom) ground scatter observed by the Goose Bay (GBR) SuperDARN radar from January to March 1994 in 0.5° elevation and 45 km range bins, sorted by radar operating frequency into four bands between 10 and 18 MHz, using the current hardware t_{diff} value of 478 ns. The Christmas Valley empirical virtual height model is overlaid on each panel in blue (Thomas & Shepherd, 2022).

the GBR radar (e.g., André et al., 1998; Milan et al., 1997). Also note the GS-flagged echoes observed at near-ranges (<500 km) across all four frequency bands are likely attributable to $\frac{1}{2}$-hop backscatter from either meteor trails or *E*-region irregularities (Makarevich, 2010; Yakymenko et al., 2015) that are misclassified due to their low velocities and spectral widths (Equation 1) and therefore not expected to match the GS component of the CV VHM.

4. Sounding Mode Data

Hughes et al. (2002) developed a special sounding mode for SuperDARN radars that utilized the ∼12 s of down-time available at the end of each standard 1 min azimuthal scan to step through a range of ∼8 equally-spaced frequencies in the 8–20 MHz band. A complete scan across all radar beams and sounding frequencies can be obtained every ∼15–30 min with this mode, and is therefore an ideal candidate for the

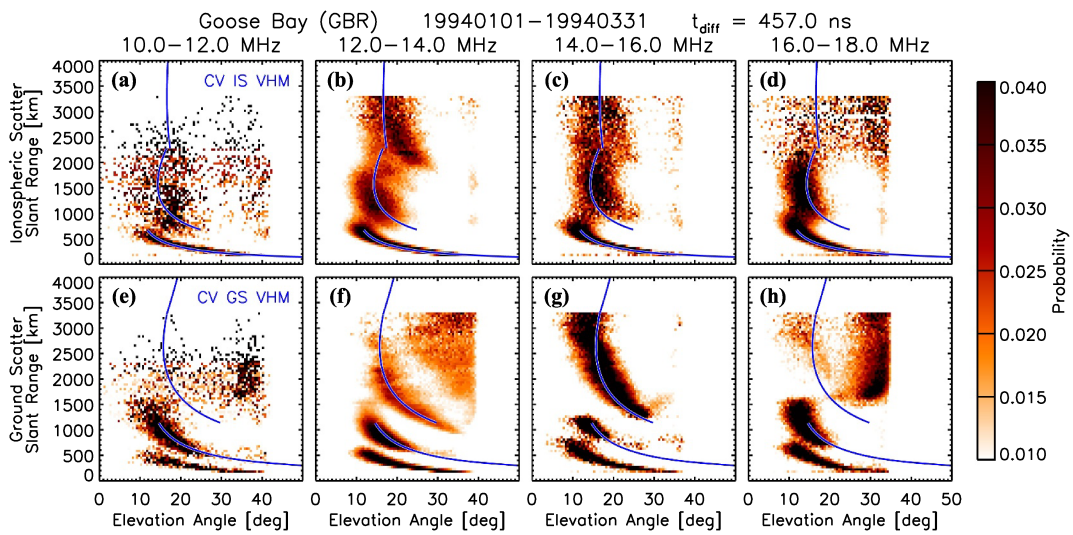

Figure 4. Joint probability distributions of elevation angle and slant range for (a–d) ionospheric scatter and (e–h) ground scatter observed by GBR in the same format as Figure 3, using a revised t_{diff} value of 457 ns.

multi-frequency calibration approach. Unfortunately, there are several challenges associated with the original sounding mode data files, including their minimally documented binary format and limited distribution. Furthermore, the elevation angles stored in the sounding data files were calculated using on-site processing software at the radars, seemingly preventing any calibration using post-processing techniques (e.g., Chisham et al., 2021).

Nevertheless, sounding mode files from a subset of radars have been recovered for various times over the years 2005–2018. By making an educated assumption about the original t_{diff} and interferometer offset values applied by the on-site FITACF software, one can convert the recorded elevation angles back to the observed phase differences (ψ_{obs}) such that post-processing calibration techniques can be applied in pursuit of a different t_{diff}. Using the notation of Shepherd (2017), this conversion takes the form

$$\psi_{obs} = 2\pi f_{\text{TX}} \left[\frac{Y}{c} \left(\cos^2 \phi_0 - \sin^2 \alpha \right)^{\frac{1}{2}} - t_{\text{diff}} \right] - 2n\pi \tag{2}$$

where f_{TX} is the radar operating frequency, c is the speed of light in free space, Y is the geometric separation between the main and interferometer antenna arrays along the array normal direction (with $+Y$ in the direction of the array normal), α is the elevation angle, ϕ_0 is the azimuthal beam direction at $\alpha = 0°$ (horizontal) set electronically by the radar hardware, and n is the integer ambiguity introduced by the separation of the main and interferometer antenna arrays. This expression is equivalent to the original elevation angle equation (e.g., André et al., 1998; Milan et al., 1997) that did not account for interferometer offsets in the X- or Z-directions.

We applied this technique to the TIGER Bruny Island (TIG) radar, which operated the sounding mode periodically from 2005 to 2011. Figure 5 shows joint probability distributions of elevation angle and slant range for GS echoes observed by TIG for the entire month of December 2005 as extracted from the sounding mode files. Each of the nine panels corresponds to a different sounding frequency, and the GS component of the CV VHM is again overlaid in blue for reference. Based on current and historical versions of the TIG information in the SuperDARN analysis software, we have assumed a t_{diff} value of 0 ns and an interferometer offset solely in the Y-direction of 100 m were used in the original on-site calculation of these elevation angles. Note the vertical striping in Figure 5 is due to the integer precision of the elevation angles (and all other parameters) stored in the sounding mode files.

The TIG elevation-range distributions appear quite reasonable at frequencies above 14.4 MHz (Figures 5f–5i). Below 14.4 MHz, however, the majority of the data at each range are mapped to very large elevation angles, similar to the GBR results in Figure 3. Applying the multi-frequency calibration technique suggests a t_{diff} value of −60 ns, the result of which can be seen in Figure 6. The GS distributions at higher frequencies remain largely unchanged from those in Figure 5, while at lower frequencies they are now in much better agreement with the CV VHM. This result (or agreement) can be understood in terms of the inherent 2π measurement ambiguity of SuperDARN interferometry, as 60 ns corresponds to the period of a 16.7 MHz wave, which lies near the middle of the upper TIG sounding frequencies (14.4 MHz/69.4 ns and 18.2 MHz/54.9 ns). An equivalent set of figures showing the pre- and post-calibrated TIG sounding mode results for IS echoes are available in the Supporting Information S1.

Beginning in April 2023, network-wide sounding mode experiments have been conducted for three consecutive days each month using an updated version of the radar control software originally developed by Hughes et al. (2002). The sounding mode data are now stored using the same format as the standard SuperDARN RawACF and FitACF files and can be processed using the open source Radar Software Toolkit (RST) (SuperDARN Data Analysis Working Group et al., 2022). The new data files also retain the observed phase differences (ψ_{obs}) for easier application of post-processing calibration techniques. Note the multi-frequency data from the ICW radar shown in Section 2 were obtained using this new sounding mode. In Table 1, we provide t_{diff} estimates for each of the participating SuperDARN radars found by applying the multi-frequency calibration approach to the 2023 sounding mode data. We hope the values in Table 1 will not only aid researchers attempting to use elevation data from these radars but also aid in future comparisons against other interferometer calibration techniques.

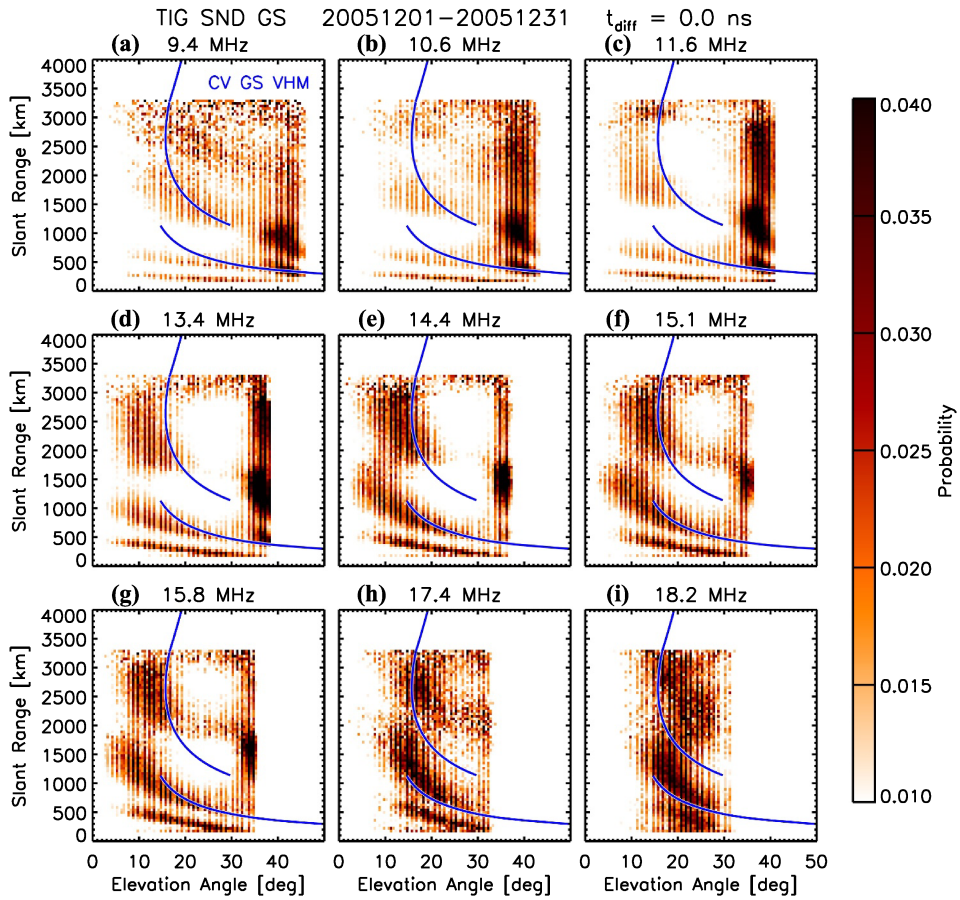

Figure 5. Joint probability distributions of elevation angle and slant range for ground scatter observed by the TIGER Bruny Island (TIG) radar during the entire month of December 2005 at 9 sounding mode frequencies, using the current hardware t_{diff} value of 0 ns. The Christmas Valley ground scatter virtual height model is overlaid on each panel in blue (Thomas & Shepherd, 2022). Note the vertical striping is due to the integer precision of the original sounding mode data format (Hughes et al., 2002).

5. Method Comparison

While t_{diff} estimates are not yet available from the other calibration techniques for comparison with the 2023 sounding mode results listed in Table 1, there are sufficient historical sounding mode files from selected radars for which methods can be compared. Here we apply the multi-frequency approach to sounding mode data from the polar Rankin Inlet (RKN) radar for September 2011 to December 2013 for comparison with t_{diff} estimates from the meteor scatter technique of Chisham (2018). Figure 7 shows monthly average values from the multi-frequency approach as red diamonds, while 10-day averages from the meteor technique are separated into 10–12 and 12–14 MHz frequency bands and shown as black squares and blue circles, respectively. Dotted lines correspond to smoothed 3-month averages of each set of t_{diff} estimates, and a dashed gray line is overlaid at 0 ns and corresponds to the current hardware value listed in the SuperDARN analysis software for RKN. Note the RKN hardware was upgraded to the digital Borealis system in September 2021 (McWilliams et al., 2023); therefore, the t_{diff} estimate of 45 ns found from the 2023 sounding experiments (Table 1) is not applicable to these older data.

The multi-frequency technique applied to the sounding mode data suggests a nearly constant t_{diff} estimate of 4 ns for RKN during this 28-month interval. The median t_{diff} estimates from the meteor calibration technique are −6.5 and −4.0 ns for the 10–12 and 12–14 MHz frequency bands, respectively. There also appears to be a slight seasonal trend in the meteor estimates in both frequency bands, which is likely to be a variation in the accuracy of the method changing with season (e.g., that the accuracy of the assumption of straight line propagation to meteor heights varies with season due to ionospheric changes). The ∼8 ns offset in t_{diff} between the multi-frequency and

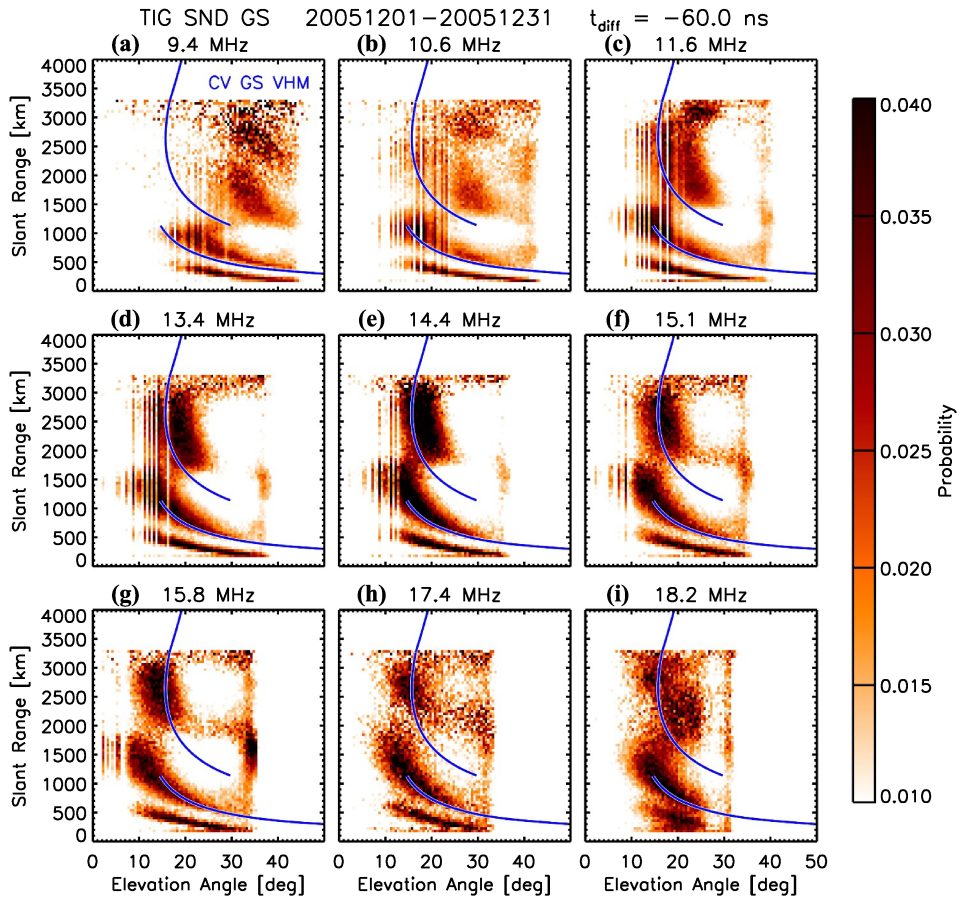

Figure 6. Joint probability distributions of elevation angle and slant range for ground scatter observed by the TIG radar during the entire month of December 2005 in the same format as Figure 5, using a revised t_{diff} value of −60 ns.

Table 1
t_{diff} Values Found by Applying Multi-Frequency Calibration to SuperDARN Radars Participating in April–December 2023 Sounding Mode Experiments

Radar name	Code	t_{diff} (ns)
Clyde River	CLY	0
Christmas Valley East	CVE	−398
Christmas Valley West	CVW	−346
Goose Bay	GBR	−63
Hokkaido East	HOK	−40
Iceland East	ICE	−300
Iceland West	ICW	−380
Inuvik	INV	0
Kapuskasing	KAP	−34
Prince George	PGR	14
Rankin Inlet	RKN	45
Saskatoon	SAS	5

meteor calibration methods is similar to previous (single-frequency) comparisons by Chisham et al. (2021) and would lead to ground range differences on the order of 50 km.

Overall, results from both calibration techniques suggest the hardware value of 0 ns listed for this time period is appropriate for all RKN operating frequencies, with an uncertainty of 4 ns. Note that for common interferometer offsets (such as at RKN), this corresponds to a typical elevation angle difference of less than 3°. However, we caution that associating uncertainties in t_{diff} to elevation angle is nonlinear; discontinuous due to the 2π phase ambiguity; and depends on frequency, beam direction, and the geometry of the interferometer array (e.g., Equation 2).

6. Discussion

The multi-frequency calibration approach improves upon the original virtual height comparison method (Chisham et al., 2021) by resolving the 2π measurement ambiguity when estimating t_{diff}. However, there remain several limitations to this technique that must be addressed. First, it requires radar measurements obtained at different operating frequencies, ideally spanning at least 5 MHz at 1 MHz intervals. Many SuperDARN radars operate in a fixed frequency band, while others use separate frequency bands for daytime and nighttime operation to try to optimize the amount of observed backscatter. It

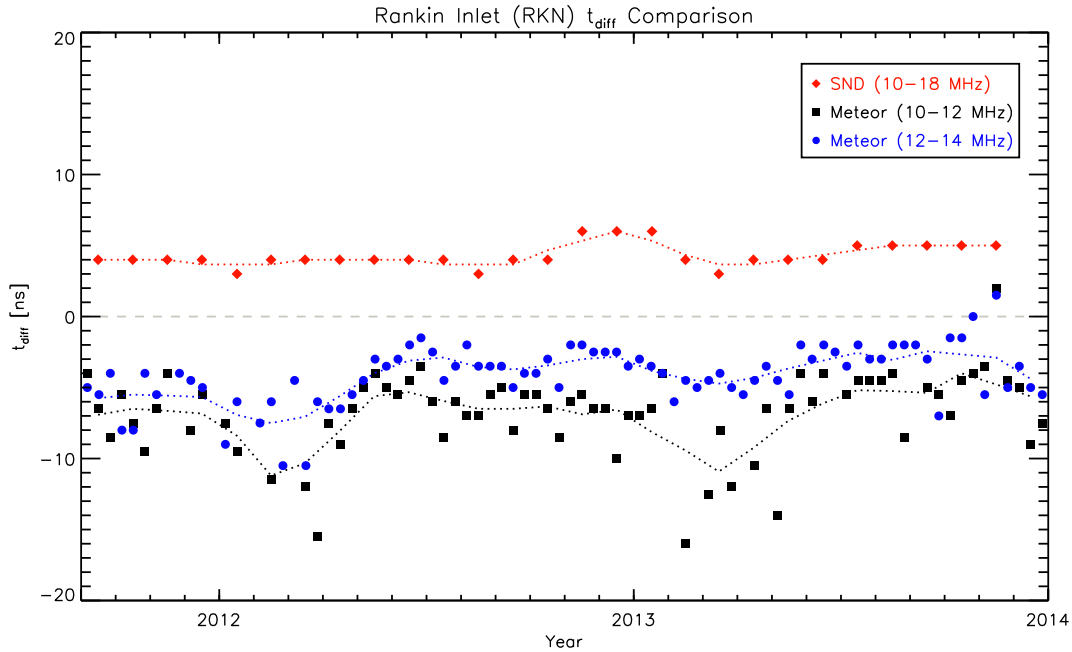

Figure 7. Comparison between the results of different t_{diff} estimation methods for the Rankin Inlet (RKN) radar from September 2011 to December 2013. Monthly average estimates from the multi-frequency sounding data (SND) are shown as red diamonds. The meteor scatter estimates of Chisham (2018) averaged over 10 days intervals for the 10–12 and 12–14 MHz frequency bands are shown as black squares and blue circles, respectively. A gray dashed line overlaid at 0 ns corresponds to the current hardware value listed for RKN in the SuperDARN analysis software.

is therefore not always possible to apply this technique to historical observations for resolving the 2π ambiguity in t_{diff} if a radar did not collect data at a range of different operating frequencies.

An outstanding issue affecting many studies involving line-of-sight SuperDARN observations is the accurate classification of ionospheric and ground backscatter sources. This is particularly an issue when a radar's observational geometry is perpendicular to the ionospheric flow direction, and also at mid-latitudes where the velocity of quiet-time ionospheric irregularities can be as low as a few tens of meters per second (Maimaiti et al., 2018; Ribeiro et al., 2012; Wang et al., 2022). Several techniques for improved classification of backscatter sources have been developed in recent years (e.g., Bland et al., 2014; Burrell et al., 2015; Kong et al., 2024; Kunduri et al., 2022; Ribeiro et al., 2011), which could be used to pre-process input data before applying the multi-frequency calibration technique to obtain improved t_{diff} estimates.

Another source of uncertainty is associated with the use of a VHM for comparison with elevation angles calculated for different values of t_{diff} at different radar operating frequencies. For example, the Chisham VHM was derived using 5 yrs of data from a single high-latitude radar (Saskatoon) during solar cycle 23, while the more recent CV VHM was derived using 5 yrs of data during solar cycle 24 from two mid-latitude radars. HF propagation conditions are known to vary based on local time, season, and solar cycle conditions. Therefore, use of the Chisham or CV VHM may not be appropriate for all radars under all geophysical conditions. More fundamentally, this technique also assumes that t_{diff} was properly calibrated when deriving the VHM. For the Chisham and CV VHMs, t_{diff} estimates were obtained using engineering measurements of the Saskatoon (SAS) and Christmas Valley radar hardware, respectively. Similar to RKN, SAS has also been upgraded to new digital hardware since collecting the data used to derive the Chisham VHM, and therefore any t_{diff} estimates from that time are not relevant to the 2023 estimate of 5 ns given in Table 1. The hardware at the CV radars has not significantly changed, however, and so the values in Table 1 are the same as those used to derive the CV VHM.

Thomas and Shepherd (2022) demonstrated that, in a climatological sense, HF propagation modes for backscatter from ionospheric irregularities are similar at both auroral and mid-latitudes. In the absence of more comprehensive VHMs, which can describe a broader range of HF propagation conditions, we believe the CV VHM is currently best suited for this multi-frequency calibration technique as it allows for the inclusion of a significantly

larger amount of input data as opposed to VHMs that only support ionospheric propagation modes. Improved performance could also be achieved by adjusting the ranges at which the VHMs change from one propagation mode to another as a function of frequency. This behavior can be clearly seen in Figure 6, where the transition between 1-hop *E*-region GS and 1-hop *F*-region GS varies from ∼1,000 km at 9.4 MHz to ∼1,700 km at 18.2 MHz, while the CV VHM transition remains fixed at 1,140 km.

Of course, the underlying principle behind the multi-frequency calibration approach (i.e., to account for the 2π measurement ambiguity in the observed phase difference) does not require the use of a VHM at all. This technique can be generalized to any of the other calibration techniques using meteor echoes or other IS or GS targets simply by comparing results at multiple (well-spaced) radar operating frequencies. Or, the multi-frequency method as described here could be applied first to provide a rough estimate of t_{diff} for all frequencies, which could then be further refined using another technique. We must also note that our approach assumes t_{diff} to be frequency independent, which has held true for all of the SuperDARN radars evaluated so far.

Finally, caution must be exercised when applying the multi-frequency (or any other) t_{diff} calibration technique to data from multi-channel "Stereo" SuperDARN radars (Lester et al., 2004). In this design, signals received by each channel follow separate paths through the radar hardware and therefore may be associated with different t_{diff} values as discussed by Chisham et al. (2021). Prior findings of frequency-dependent t_{diff} estimates for the Stereo Hankasalmi radar (e.g., Burrell et al., 2016) are likely a channel-dependent feature instead.

7. Summary

In this study we have presented a new approach for calibrating SuperDARN interferometer measurements that can be applied to even the earliest available data. Using both ionospheric and ground backscatter observations from a diverse set of radar operating frequencies, one can identify the time delay correction factor (t_{diff}) associated with the electrical path length difference between the antenna arrays that best agrees with empirical HF propagation characteristics at all frequencies. We have successfully applied this technique to obtain t_{diff} estimates for a dozen radars using multi-frequency observations from the past year. By regularly conducting multi-frequency sounding campaigns, this technique can allow for continuous calibration of elevation angles and therefore improved geolocation of all SuperDARN backscatter observations.

Data Availability Statement

The raw SuperDARN data used in this study are available from the British Antarctic Survey SuperDARN data mirror (https://www.bas.ac.uk/project/superdarn/#data). While data for this study were accessed from the British Antarctic Survey, they may also be obtained from the Canadian Federated Research Data Repository (FRDR) at https://www.frdr-dfdr.ca/repo/collection/superdarn (Super Dual Auroral Radar Network, 2021). The Radar Software Toolkit to read and process the SuperDARN data can be downloaded from Zenodo (SuperDARN Data Analysis Working Group et al., 2022).

Acknowledgments
This research was funded by the Office of Naval Research under Grant N000142312109, by the Air Force Research Laboratory under Grant FA94532220027, and by the National Science Foundation under Grants OPP-1836426 and AGS-1934997. Gareth Chisham was funded as part of the British Antarctic Survey (BAS) Polar Science for a Sustainable Planet programme and by the UK NERC Grant NE/R016038/1. The authors acknowledge the use of SuperDARN data. SuperDARN is a collection of radars funded by the national scientific funding agencies of Australia, Canada, China, France, Italy, Japan, Norway, South Africa, United Kingdom, and the United States of America. Operation of the Iceland West and Goose Bay radars is supported by the National Science Foundation. The authors acknowledge the use of data provided by the TIGER Consortium Partners and their supporting funding organizations: Australian Research Council and US AFOSR. Operation of the Rankin Inlet radar is supported by the Canada Foundation for Innovation, Canadian Space Agency, and Province of Saskatchewan.

References

André, D., Sofko, G. J., Baker, K., & MacDougall, J. (1998). SuperDARN interferometry: Meteor echoes and electron densities from groundscatter. *Journal of Geophysical Research*, *103*(A4), 7003–7015. https://doi.org/10.1029/97JA02923

Baker, K. B., & Greenwald, R. A. (1988). The vertical angle of arrival of high-frequency signals propagating from Thule to Goose Bay. *Johns Hopkins APL Technical Digest*, *9*(2), 121–130.

Bland, E. C., McDonald, J., de Larquier, S., & Devlin, J. C. (2014). Determination of ionospheric parameters in real time using SuperDARN HF radars. *Journal of Geophysical Research: Space Physics*, *119*(7), 5830–5846. https://doi.org/10.1002/2014JA020076

Bristow, W. A., Lyons, L. R., Nishimura, Y., Shepherd, S. G., & Donovan, E. F. (2022). High-latitude plasma convection based on SuperDARN observations and the locally divergence free criterion. *Journal of Geophysical Research: Space Physics*, *127*(12), e2022JA030883. https://doi.org/10.1029/2022JA030883

Burrell, A. G., Milan, S. E., Perry, G. W., Yeoman, T. K., & Lester, M. (2015). Automatically determining the origin direction and propagation mode of high-frequency radar backscatter. *Radio Science*, *50*(12), 1225–1245. https://doi.org/10.1002/2015RS005808

Burrell, A. G., Yeoman, T. K., Milan, S. E., & Lester, M. (2016). Phase calibration of interferometer arrays at high-frequency radars. *Radio Science*, *51*(9), 1445–1456. https://doi.org/10.1002/2016RS006089

Chisham, G. (2018). Calibrating SuperDARN interferometers using meteor backscatter. *Radio Science*, *53*(6), 761–774. https://doi.org/10.1029/2017RS006492

Chisham, G., Burrell, A. G., Marchaudon, A., Shepherd, S. G., Thomas, E. G., & Ponomarenko, P. (2021). Comparison of interferometer calibration techniques for improved SuperDARN elevation angles. *Polar Science*, *28*, 100638. https://doi.org/10.1016/j.polar.2021.100638

Chisham, G., & Freeman, M. P. (2013). A reassessment of SuperDARN meteor echoes from the upper mesosphere and lower thermosphere. *Journal of Atmospheric and Solar-Terrestrial Physics*, *102*, 207–221. https://doi.org/10.1016/j.jastp.2013.05.018

Chisham, G., Lester, M., Milan, S. E., Freeman, M. P., Bristow, W. A., Grocott, A., et al. (2007). A decade of the Super Dual Auroral Radar Network (SuperDARN): Scientific achievements, new techniques and future directions. *Surveys in Geophysics*, *28*(1), 33–109. https://doi.org/10.1007/s10712-007-9017-8

Chisham, G., Yeoman, T. K., & Sofko, G. J. (2008). Mapping ionospheric backscatter measured by the SuperDARN HF radars – Part 1: A new empirical virtual height model. *Annales Geophysicae*, *26*(4), 823–841. https://doi.org/10.5194/angeo-26-823-2008

Cousins, E. D. P., Matsuo, T., & Richmond, A. D. (2013). SuperDARN assimilative mapping. *Journal of Geophysical Research: Space Physics*, *118*(12), 7954–7962. https://doi.org/10.1002/2013JA019321

Fiori, R. A. D., Boteler, D. H., Koustov, A. V., Haines, G. V., & Ruohoniemi, J. M. (2010). Spherical cap harmonic analysis of Super Dual Auroral Radar Network (SuperDARN) observations for generating maps of ionospheric convection. *Journal of Geophysical Research*, *115*(A7), A07307. https://doi.org/10.1029/2009JA015055

Greenwald, R. A., Baker, K. B., Dudeney, J. R., Pinnock, M., Jones, T. B., Thomas, E. C., et al. (1995). DARN/SuperDARN: A global view of the dynamics of high-latitude convection. *Space Science Reviews*, *71*(1), 761–796. https://doi.org/10.1007/BF00751350

Greenwald, R. A., Baker, K. B., Hutchins, R. A., & Hanuise, C. (1985). An HF phased-array radar for studying small-scale structure in the high-latitude ionosphere. *Radio Science*, *20*(1), 63–79. https://doi.org/10.1029/RS020i001p00063

Greenwald, R. A., Frissell, N., & de Larquier, S. (2017). The importance of elevation angle measurements in HF radar investigations of the ionosphere. *Radio Science*, *52*(3), 305–320. https://doi.org/10.1002/2016RS006186

Greenwood, R. I., Parkinson, M. L., Dyson, P. L., & Schulz, E. W. (2011). Dominant ocean wave direction measurements using the TIGER SuperDARN systems. *Journal of Atmospheric and Solar-Terrestrial Physics*, *73*(16), 2379–2385. https://doi.org/10.1016/j.jastp.2011.08.006

Hughes, J. M., Bristow, W. A., Greenwald, R. A., & Barnes, R. J. (2002). Determining characteristics of HF communications links using SuperDARN. *Annales Geophysicae*, *20*(7), 1023–1030. https://doi.org/10.5194/angeo-20-1023-2002

Kong, X., Liu, E., Shi, S., & Chen, F. (2024). The implementation of deep clustering for SuperDARN backscatter echoes. *Advances in Space Research*, *74*(1), 243–254. https://doi.org/10.1016/j.asr.2024.03.039

Kunduri, B. S. R., Baker, J. B. H., Ruohoniemi, J. M., Thomas, E. G., & Shepherd, S. G. (2022). An examination of SuperDARN backscatter modes using machine learning guided by ray-tracing. *Space Weather*, *20*(9), e2022SW003130. https://doi.org/10.1029/2022SW003130

Lester, M., Chapman, P. J., Cowley, S. W. H., Crooks, S. J., Davies, J. A., Hamadyk, P., et al. (2004). Stereo CUTLASS—A new capability for the SuperDARN HF radars. *Annales Geophysicae*, *22*(2), 459–473. https://doi.org/10.5194/angeo-22-459-2004

Maimaiti, M., Baker, J. B. H., Ruohoniemi, J. M., & Ribeiro, A. J. (2018). Statistical study of nightside quiet time midlatitude ionospheric convection. *Journal of Geophysical Research: Space Physics*, *123*(3), 2228–2240. https://doi.org/10.1002/2017JA024903

Makarevich, R. A. (2010). On the occurrence of high-velocity E-region echoes in SuperDARN observations. *Journal of Geophysical Research*, *115*(A7), A07302. https://doi.org/10.1029/2009JA014698

McDonald, A. J., Whittington, J., de Larquier, S., Custovic, E., Kane, T. A., & Devlin, J. (2013). Elevation angle-of-arrival determination for a standard and a modified SuperDARN HF radar layout. *Radio Science*, *48*(6), 709–721. https://doi.org/10.1002/2013RS005157

McWilliams, K. A., Detwiller, M., Kotyk, K., Krieger, K., Rohel, R., Billett, D. D., et al. (2023). Borealis: An advanced digital hardware and software design for SuperDARN radar systems. *Radio Science*, *58*(3), e2022RS007591. https://doi.org/10.1029/2022RS007591

Milan, S. E., Jones, T. B., Robinson, T. R., Thomas, E. C., & Yeoman, T. K. (1997). Interferometric evidence for the observation of ground backscatter originating behind the CUTLASS coherent HF radars. *Annales Geophysicae*, *15*(1), 29–39. https://doi.org/10.1007/s00585-997-0029-y

Nishitani, N., Ruohoniemi, J. M., Lester, M., Baker, J. B. H., Koustov, A. V., Shepherd, S. G., et al. (2019). Review of the accomplishments of mid-latitude Super Dual Auroral Radar Network (SuperDARN) HF radars. *Progress in Earth and Planetary Science*, *6*(1), 27. https://doi.org/10.1186/s40645-019-0270-5

Ponomarenko, P. V., Nishitani, N., Oinats, A. V., Tsuya, T., & St. Maurice, J.-P. (2015). Application of ground scatter returns for calibration of HF interferometry data. *Earth Planets and Space*, *67*(1), 138. https://doi.org/10.1186/s40623-015-0310-3

Ponomarenko, P. V., St. Maurice, J.-P., Hussey, G. C., & Koustov, A. V. (2010). HF ground scatter from the polar cap: Ionospheric propagation and ground surface effects. *Journal of Geophysical Research*, *115*(A10), A10310. https://doi.org/10.1029/2010JA015828

Ponomarenko, P. V., St. Maurice, J.-P., & McWilliams, K. A. (2018). Calibrating HF radar elevation angle measurements using *E* layer backscatter echoes. *Radio Science*, *53*(11), 1438–1449. https://doi.org/10.1002/2018RS006638

Ribeiro, A. J., Ruohoniemi, J. M., Baker, J. B. H., Clausen, L. B. N., Greenwald, R. A., & Lester, M. (2012). A survey of plasma irregularities as seen by the midlatitude Blackstone SuperDARN radar. *Journal of Geophysical Research*, *117*(A2), A02311. https://doi.org/10.1029/2011JA017207

Ribeiro, A. J., Ruohoniemi, J. M., Baker, J. B. H., de Larquier, S., & Greenwald, R. A. (2011). A new approach for identifying ionospheric backscatter in midlatitude SuperDARN HF radar observations. *Radio Science*, *46*(4), RS4011. https://doi.org/10.1029/2011RS004676

Ruohoniemi, J. M., & Baker, K. B. (1998). Large-scale imaging of high-latitude convection with Super Dual Auroral Radar Network HF radar observations. *Journal of Geophysical Research*, *103*(A9), 20797–20811. https://doi.org/10.1029/98JA01288

Shand, B. A., Milan, S. E., Yeoman, T. K., Chapman, P. J., Wright, D. M., Jones, T. B., & Pederson, L. T. (1998). CUTLASS HF radar observations of the Odden ice tongue. *Annales Geophysicae*, *16*, 280–282. https://doi.org/10.1007/s00585-997-0063-9

Shepherd, S. G. (2017). Elevation angle determination for SuperDARN HF radar layouts. *Radio Science*, *52*(8), 938–950. https://doi.org/10.1002/2017RS006348

SuperDARN Data Analysis Working Group, Thomas, E. G., Reimer, A. S., Bland, E. C., Burrell, A. G., Grocott, A., Ponomarenko, P. V., et al. (2022). SuperDARN Radar Software Toolkit (RST) 5.0 [Software]. *Zenodo*. https://doi.org/10.5281/zenodo.7467337

Super Dual Auroral Radar Network. (2021). SuperDARN 1994 DAT [Dataset]. *Federated Research Data Repository*. https://doi.org/10.20383/102.0470

Thomas, E. G., & Shepherd, S. G. (2022). Virtual height characteristics of ionospheric and ground scatter observed by mid-latitude SuperDARN HF radars. *Radio Science*, *57*(6), e2022RS007429. https://doi.org/10.1029/2022RS007429

Wang, W., Zhang, J. J., Wang, C., Nishitani, N., Yan, J. Y., Lan, A. L., et al. (2022). Statistical characteristics of mid-latitude ionospheric irregularities at geomagnetic quiet time: Observations from the Jiamusi and Hokkaido East SuperDARN HF radars. *Journal of Geophysical Research: Space Physics*, *127*(1), e2021JA029502. https://doi.org/10.1029/2021JA029502

Yakymenko, K. N., Koustov, A. V., & Nishitani, N. (2015). Statistical study of midlatitude E region echoes observed by the Hokkaido SuperDARN HF radar. *Journal of Geophysical Research: Space Physics*, *120*(11), 9959–9976. https://doi.org/10.1002/2015JA021685